LARGE SYNOPTIC SURVEY TELESCOPE
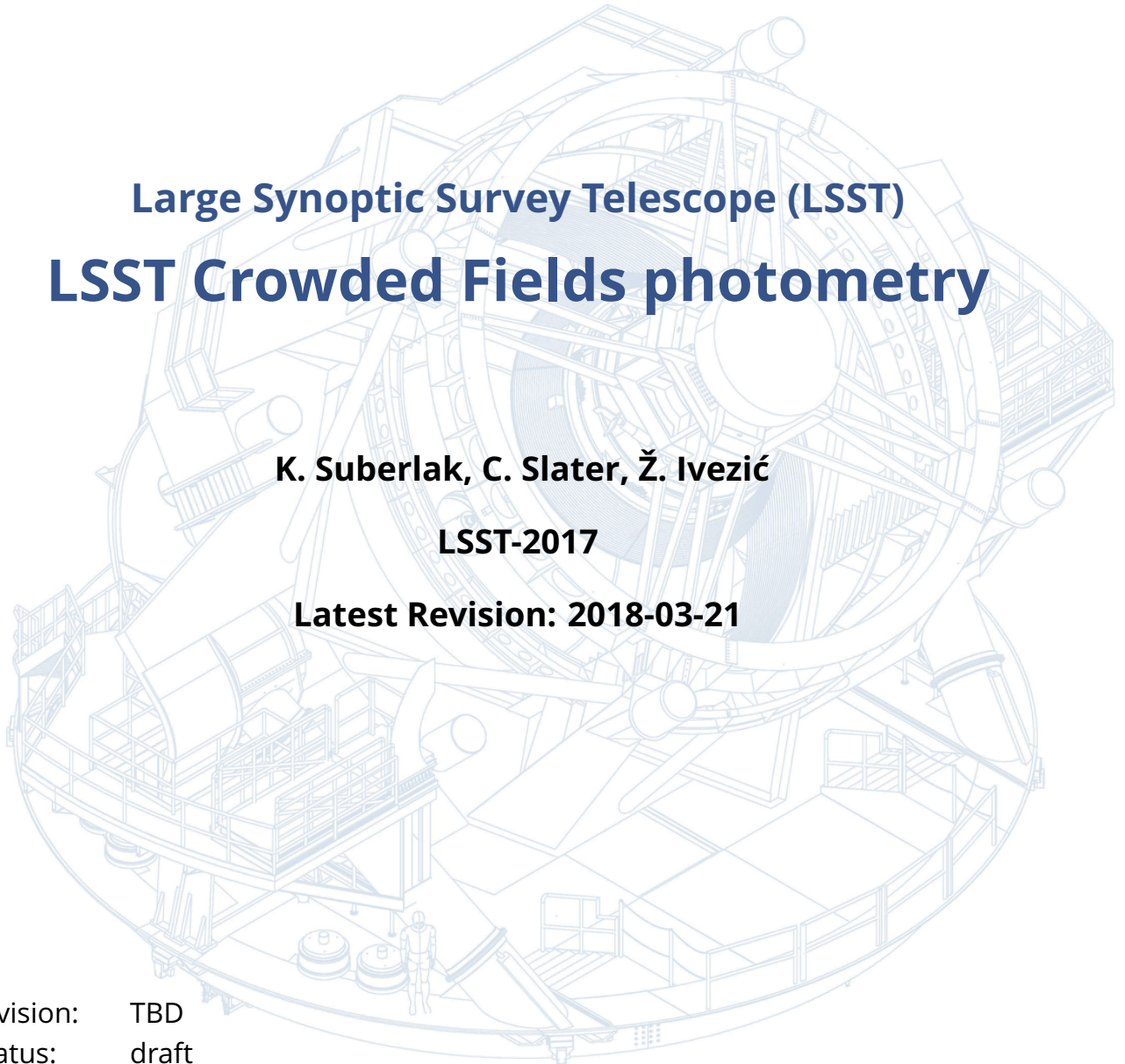
Large Synoptic Survey Telescope (LSST)

LSST Crowded Fields photometry

K. Suberlak, C. Slater, Ž. Ivezić

LSST-2017

Latest Revision: 2018-03-21

revision: TBD
status: draft

Abstract

A report on the performance of current LSST Stack pipelines in crowded stellar fields. We use the DECAPS data to define the photometry and astrometry quality assurance metrics.

In the top 10% region, where DECAPS detects 200 000 sources per sq.deg., the mean LSST-DECAPS completeness in 18-20 mag is 80%, and it drops to 50% at 21.5 mag. For the same visit, the DECAPS 5σ limiting depth is 23 mag.

For a top 2% region, within the exclusion zone, in which DECAPS detects 500 000 sources per sq.deg., the mean completeness in 18-20 mag of LSST to DECAPS source-by-source is 78%, and it drops to 50% at 20.2 mag. For the same visit, the DECAPS 5σ limiting depth is 23.2 mag.

The systematic offset in photometry (the difference between the median photometric uncertainty and the measure of internal photomtric repeatability) at 21 mag for the density of 200 000 sources per sq.deg. is 0.06 mag.

The LSST photometry is consistent with DECAPS. Above 19th mag, LSST and DE-CAPS are in systematics-dominated regime, consistent at 0.02 mag level. At fainter magnitudes, the scatter between LSST and DECAPS is less than the photometric uncertainty.

The spread of astrometric repeatability for LSST epoch-to-epoch is at the level of 10-30 miliarcsec, and is not strongly dependent on stellar crowdedness.

Change Record

Version	Date	Description	Owner name
1	2018-03-20	Final draft.	Krzysztof Suberlak

Contents

1   Introduction

We report on the performance of the Large Scale Synoptic Telescope (LSST) science pipelines[1], also known as 'the LSST stack', in the stellar fields of varying levels of source crowdedness.

The LSST will sample every night on average over 500 regions in the sky , delivering terabytes of raw data in need of processing, including photometric and astrometric calibration, to deliver a calibrated exposure image, as well as a source catalog, among image products[2] [8].

The survey sky is composed of regions very diverse in terms of stellar density, or crowdedness. Assuming the single-visit depth of 24.5 mag, the stellar density ranges from high density low-galactic latitude regions that have tens of millions of sources per square degree, to low-density regions towards the Galactic poles with less than thousand sources per square degree.

Deblending and successful photometry is an inherent part of any astronomical data processing pipeline. There exists a body of research answering questions that are specific to crowded stellar fields, eg. how many beams do we need per source [3], or how the crowded fields photometry can be approached in the era of large telescopes [9]. Other studies involving Hyper-Suprime CAM pipeline (developed in parallel with the LSST Stack) recognized that the deeper the survey, the higher the stellar densities encountered, and therefore, the more challenging the process of deblending photometry [1].

In this report we compare the 'out-of-the-box' LSST Stack processing pipeline, to the DECAm [Galactic] Plane Survey (DECAPS) pipeline deveolped by Schlafly et al. [10].

To test performance of pipelines at different levels of stellar crowdedness, we choose regions of the sky at various densities based on the Galfast simulation of the night sky (Sec. 2).

Given the expected stellar density as a function of position on the sky, we selected DECAPS fields, and processed them with LSST pipelines (Sec. 3).

We compare the results of the LSST and DECAPS processing of the same visits by cross-matching the catalogs and comparing source counts, photometry (Sec. 4), and astrometry

---

[1] https://pipelines.lsst.io
[2] http://ls.st/LSE-163

(Sec. 6). We summarize the key results and suggest future work in Sec. 7.

2   Identifying density regions

To identify regions representing different stellar densities we use the Galfast simulated stellar density map prepared as part of Metrics Analysis Framework[3] by P. Yoachim and L. Jones[4].

The resulting dataset describes the simulated sky, divided into 49152 healpixels. Each healpixel contains 64 magnitude bins between 15 and 28 mag, each bin storing the cumulative count of sources per square degree[5]. We select the bin corresponding to the LSST single-visit depth of r=24.5. For each healpixel we find the fraction of pixels that have a higher stellar count (see Fig. 1).

Since by definition each healpixel has an equal area, the fraction of pixels corresponds to the fraction of the sky area. We choose to describe the level of stellar crowdedness by the percentage of the sky that has a higher density. Thus eg. '5%' density means that only 1 in 100 pixels has a higher density (see Fig. 1, 2).

3   DECam Plane Survey

To test the performance of the LSST Stack with real data, we used the Dark Energy Camera (DECam) imaging, taken as part of the DECam Plane Survey (DECAPS) [10], at the 4-m Cerro Tololo Inter-American Observatory telescope (CTIO)[6]. Each DECAPS image plane is tiled by a mosaic of 62 CCDs, each 2046x4094 px, 0.27 "/px[7]. The FOV of full mosaic is 2.2°wide - several times bigger than the full moon - which makes it comparable to the LSST 3.5°field of view. All DECAPS single-epoch images were processed with the DECAPS pipeline, resulting in single-epoch catalogs[8]. The details of DECAPS pipeline can be found in Schlafly et al. 2017 [10], but it was specifically designed for crowded field photometry, performing DAOPhot-like procedure [12], without employing DAOPhot. The algorithm performs repeated source detection,

---

[3]https://www.lsst.org/scientists/simulations/maf
[4]sims_maf/python/lsst/sims/maf/maps/createStarDensitymap.py
[5]Healpix stands for Hierarchical Equal Area isoLatitude Pixelizationhttp://healpix.sourceforge.net[2]
[6]see http://www.ctio.noao.edu/noao/node/1033
[7]See Fig.4-3 in the NOAO Data Handbook [11]
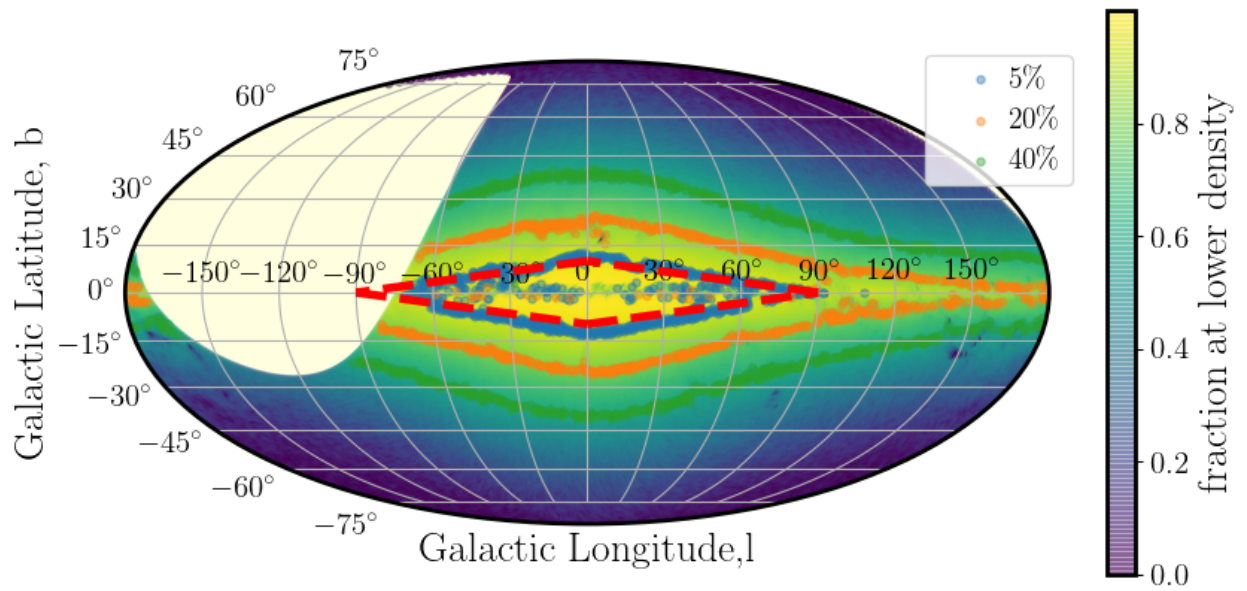[8]All available via http://decaps.skymaps.info/catalogs.html

FIGURE 1: Galfast healpixels plotted in galactic coordinates in Mollweide projection. The brightest regions correspond to highest stellar densities. The blue, orange, and green points correspond to healpixels in given density brackets (top 5%, 20%, 40%). Note that the galactic exclusion zone, marked by red dashed lines, almost exactly traces the top 5% density contour. As expected, the highest density regions are located close to the galactic bulge, and regions of approximately constant stellar density trace isophotes of the Milky Way. The few 20% regions close to the galactic equator correspond to high extinction regions that appear to have less counts due to interstellar dust. The missing part at $\delta > 40°$ is not observable from the southern location of Cerro Pachón, hence excluded from the simulation.
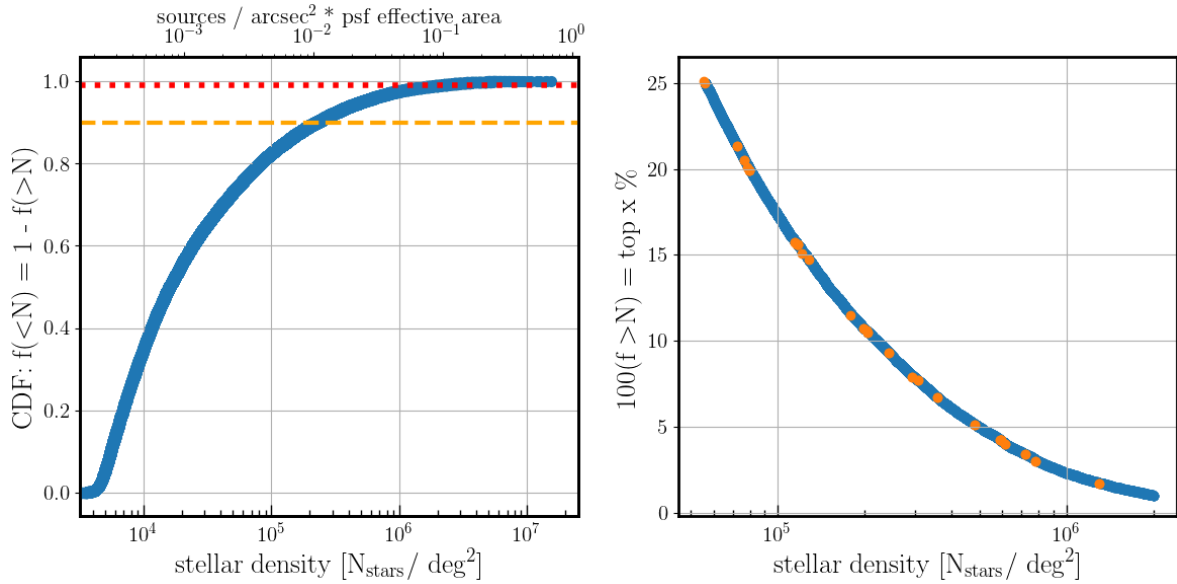
FIGURE 2: Using the Galfast sky simulation to choose DECAPS fields sampling different density regions. The left panel shows the fraction of the sky at a smaller density as a function of the stellar density. It is equivalent to the cumulative area of the sky up to given density. Given the stellar density per simulated healpixel, we count the number of healpixels at greater density. Normalized to the number of pixels, given their equal area, it corresponds to the fraction of the sky at greater stellar density. Horizontal dashed lines illustrate selecting pixels at top 1% or 10% density. The right panel focuses on the top 25% of density. It implies that according to the simulation , the density of 200 000 stars per sq.deg. corresponds to 5% of the sky, and only 1% of the sky has more than 1 mln stars per sq.deg. The upper axis represents the dimensionless density parameter $N_{beam} = N_{stars}/arcsec^2 * A_{PSF}$, with the PSF effective area $A_{PSF} = 0.64\,''$.

subtraction, and re-detection, which is different from the LSST pipeline. DECAPS pipeline simultaneously solves for the positions and fluxes for all stars for a small fragment of the CCD (see Sec.4 in [10]). The headers of all DECAPS catalogs, assembled into the image database with information about single-visit exposure time, filter, time of observation, position, were used to select fields in u,g,r filter, with exposure between 90 and 120 sec (to match the LSST 30 sec single-visit depth in r). Of these, we chose visits representative of given stellar densities based on the Galfast simulation (see Fig. 3). Postage stamp miniatures (Fig. 4) show that we indeed sample vastly diffferent densities. Comparing DECAPS to Galfast counts (Fig. 5) we find that although the simulation may be not more accurate than up to a actor of a few, it is nevertheless useful for defining density regions.
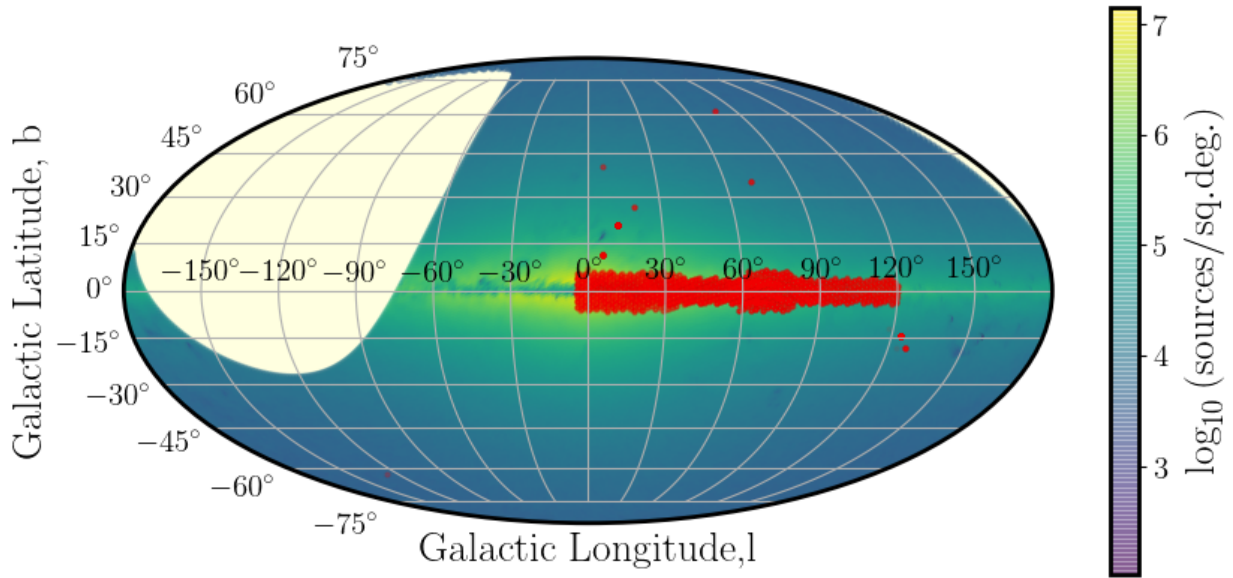

FIGURE 3: DECAPS fields (red) plotted on top of the Galfast simulated stellar density map (counts up to r<24.5). Cross-matching DECAPS catalog to Galfast simulation we selected visits representative of diverse range of stellar densities.

4   LSST Processing of DECAPS data

Calibrated DECAPS imaging was processed with the LSST Science Pipelines installed on the LSST-dev machine at the NCSA[9], using the Stack version d_2017_10_27[10] processCcd.py and the standard Stack configuration.

---

[9]lsst-dev01.ncsa.illinois.edu (141.142.237.49) OS: CentOS 7.4.1708 HW: Dell Inc. CPU: 48x 2.60GHz RAM: 252 GB

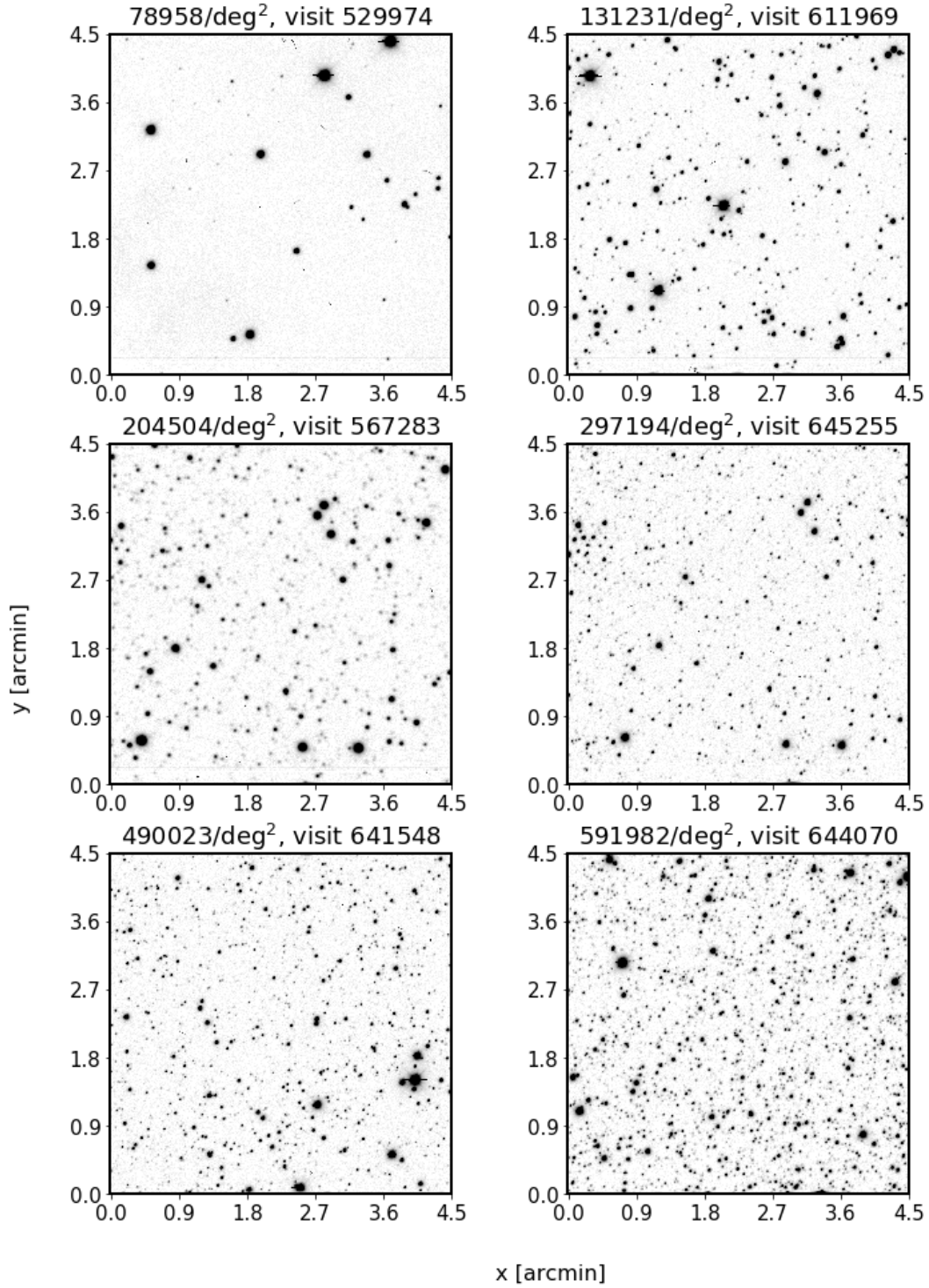[10]https://eups.lsst.codes/stack/src/tags/

FIGURE 4: Illustration of regions of different stellar count in the cleaned DECAPS single-epoch catalogs. As shown on Fig. 5, the Galfast count does not always correspond 1:1 to the DE-CAPS stellar count. For this reason we ordered DECAPS fields in terms of DECAPS source count rather than Galfast densities.
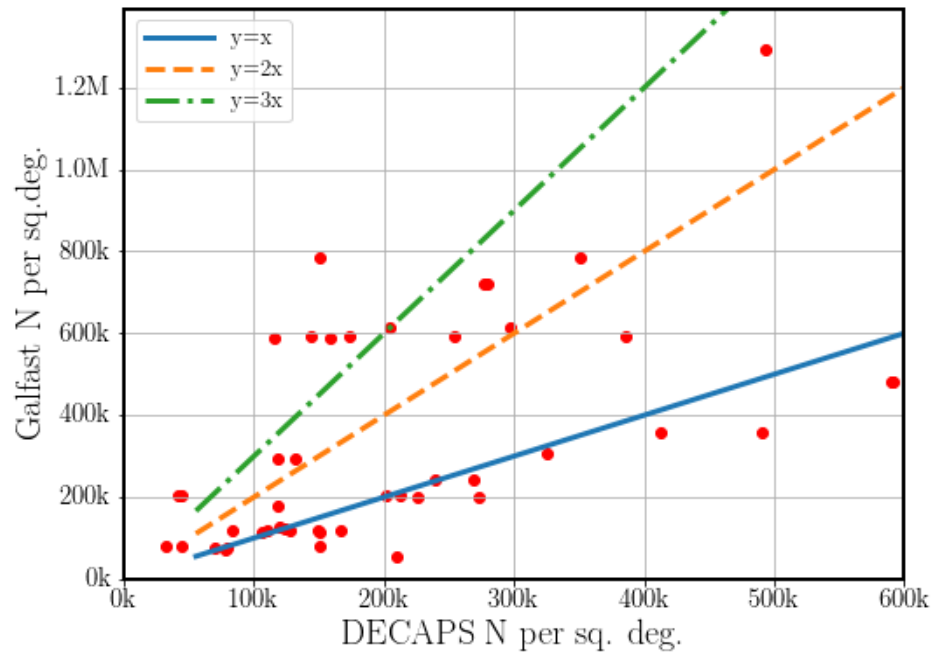
FIGURE 5: Comparison of DECAPS counts to Galfast simulated stellar counts. Overplotted are the line of equivalence y=x, and its multipicities (2x,3x). Part of the reason for discrepancy could be the order-of-magnitude nature of the experiment - Galfast counts here assume the single-visit depth of 24.5 mag in r-band. The DECAPS exposure time ($\approx$100 sec) and filter (g, or r) were chosen to mimic that depth as closely as possible, but the regions targeted include much extinction, which means that in some cases DECAPS counts may be less than what is implied by the simulation. However, there is a number of fields that lie along the blue line, implying that in some cases the Galfast counts were very close to the measured DECAPS counts.

Transferring the resulting source catalogs and image files to a local machine we analyzed the output of LSST processing with jupyter notebooks and custom python tools[11]

Initially both DECAPS and LSST source catalogs contain good detections, as well as sources that are spurious, have a low S/N, or are flagged due to some other detection/processing issue. To clean both catalogs we used the DECAPS source flags, LSST source flags, and LSST image mask information.

First we compared whether the DECAPS source flags are consistent with the LSST image mask (Table 2). Confirming that they are, we decided to clean the DECAPS catalog with the DECAPS source level flags, removing edge detections, cosmic rays, or saturation spikes (see Table 3).

We followed a similar procedure with LSST source catalogs, removing sources flagged as 'edge' or 'interpolatedCenter'[12]. Moreover, only in case of LSST catalog we are provided with the deblender-level information with 'parentId' and 'nchild' information for each source. Since the LSST pipeline deblends sources in a similar fashion to the SDSS Imaging Pipeline[13], based on 'parentId' and 'nchild' we retain only successfully deblended children, or isolated parents (see Table 5, and Fig.6).

Finally, for both LSST and DECAPS catalogs we made a quality cut on S/N, keeping only sources where S/N > 5.

5   Source detection and photometry

We compare the LSST and DECAPS source catalogs in terms of source detection completeness and photometric accuracy. Considering the clean catalog source counts up to a given magnitude, we find that DECAPS catalogs contain more sources, which is especially noticeable at higher densities, with largest contribution from sources above 22 mag (Fig. 8).

---

[11] Remote jupyter notebook access, which will be part of the Data Access Center, is not supported yet, as of early 2018.

[12] This is similar to the example in Sec.4 of SDSS Image Processing I: The Deblender [4]. Other flags would remove too many sources that have only small defects, eg. a bright source with a cosmic ray across its footprint can be flagged as 'interpolated', while any source which has even one bad pixel in the footprint would be flagged as 'bad' (Table 4).

[13] SDSS Image Processing I: The Deblender [4], SDSS Image Processing II: The Photo Pipelines [5], [7], and [6]

TABLE 2: LSST pixel mask. The decision is with reference to comparing specific LSST mask information to the DECAPS source flags.

Bit position	Description	Decision
0	bad	Remove
1	saturated	Remove
2	interpolated	Remove
3	cosmic ray	Remove
4	edge	Remove
5	detected	Keep
6	detected negative	Remove
7	suspect	Remove
8	no data	Remove

TABLE 3: DECAPS source flags.

Bit position	Description	Decision
1	Bad pixel	Remove
3	Saturated	Remove
4	Bleed trail	Remove
5	Cosmic ray	Remove
6	Low weight	Remove
8	Long streak	Remove
20	Additional bad pixel	Remove
21	Nebulosity	Keep
22	S7 amplifier B	Remove

TABLE 4: LSST source flags.

name	explanation
flag	general failure flag, set if anything went wrong
offimage	Source center is off image
edge	Source is outside usable exposure region
interpolated	Interpolated pixel in the Source footprint
saturated	Saturated pixel in the Source footprint
cr	Cosmic ray in the Source footprint
bad	Bad pixel in the Source footprint
suspect	Source's footprint includes suspect pixels
interpolatedCenter	Interpolated pixel in the Source center
saturatedCenter	Saturated pixel in the Source center
crCenter	Cosmic ray in the Source center
suspectCenter	Source's center is close to suspect pixels
flag	General Failure Flag

TABLE 5: Summary of possible parentId and nchild combinations for blended sources in the LSST Science Pipeline. An example count in the final column is provided for visit 525814, a top 20% density region, which has the raw source count 235307. For that visit 16811 sources had bad flags, 49901 had S/N < 5, and in total 163093 were kept in the clean catalog.

parentID	nchild	type	decision	count
0	0	parent: isolated source	keep	104406
0	>0	blended source	remove	26981
!=0	0	deblended child	keep	103920
!=0	>0	failure case	remove	0
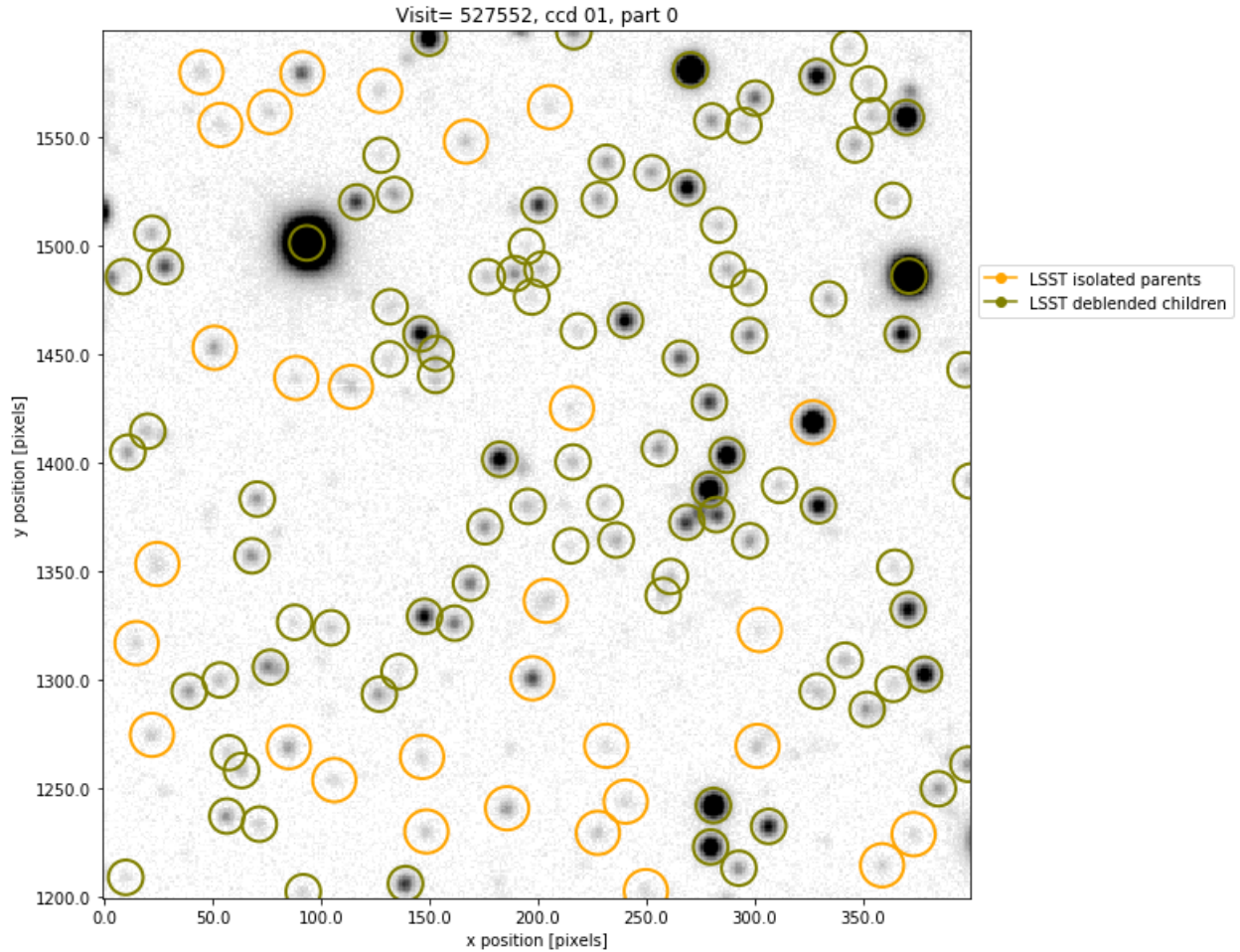
FIGURE 6: We illustrate the sources as reported by the LSST pipeline for a small region of CCD01 of visit 527552. A source may be reported as an isolated source (yellow), or a successfully deblended child (green). In this analysis we only keep isolated parents or deblended children.
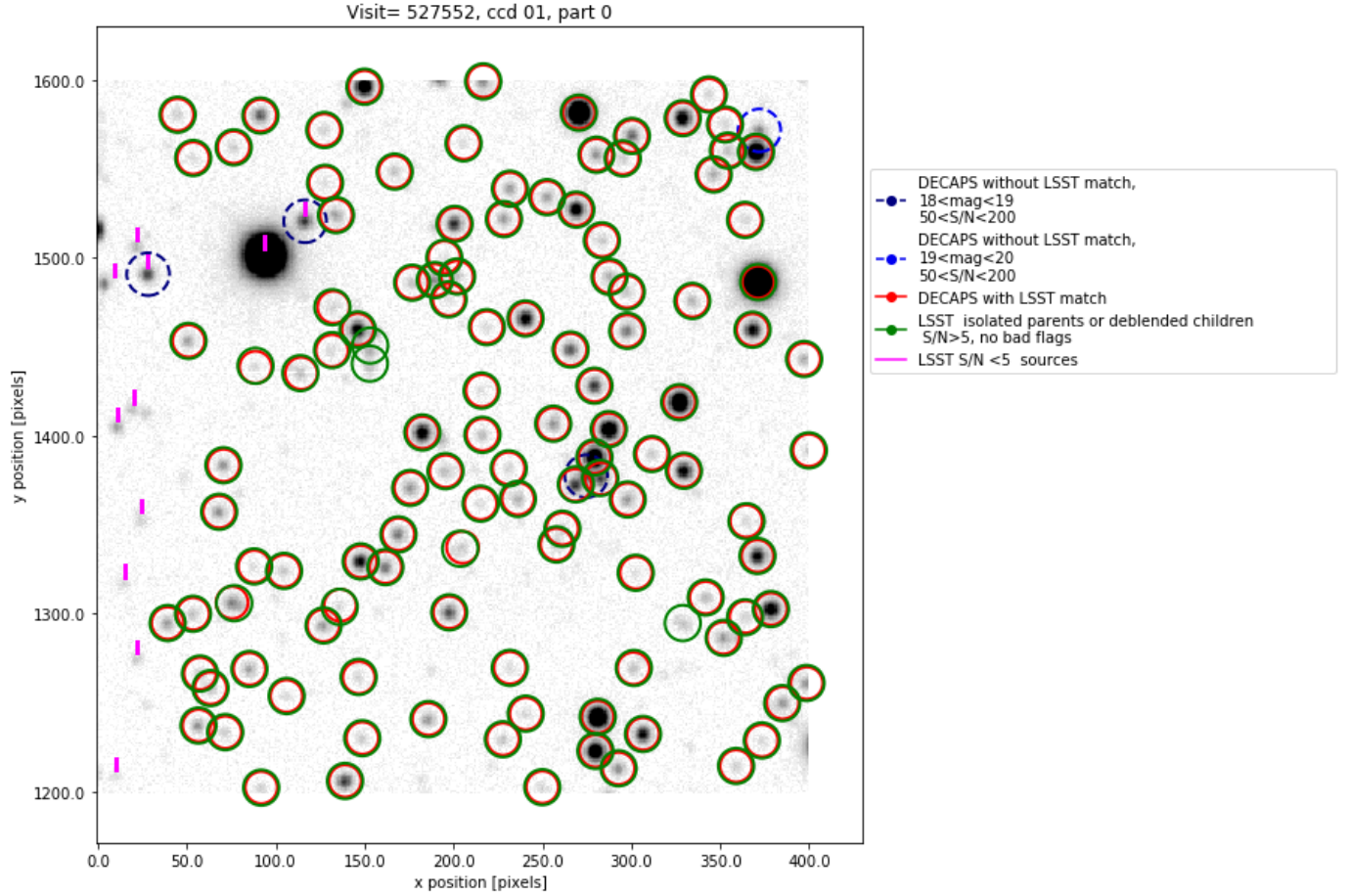
FIGURE 7: The same region as on Fig. 6. Green circles mark the position of retained LSST sources: isolated parents, or deblended children, with S/N > 5, and no bad flags. Red circles mark the position of DECAPS detections with an LSST match. Vertical magenta dashes indicate LSST sources with S/N < 5. Blue dashed circles mark location of DECAPS source without an LSST match. Note that eg. at (x,y) = 50,1490 an LSST source was detected, but since its S/N < 5 it was not kept in the clean LSST catalog.
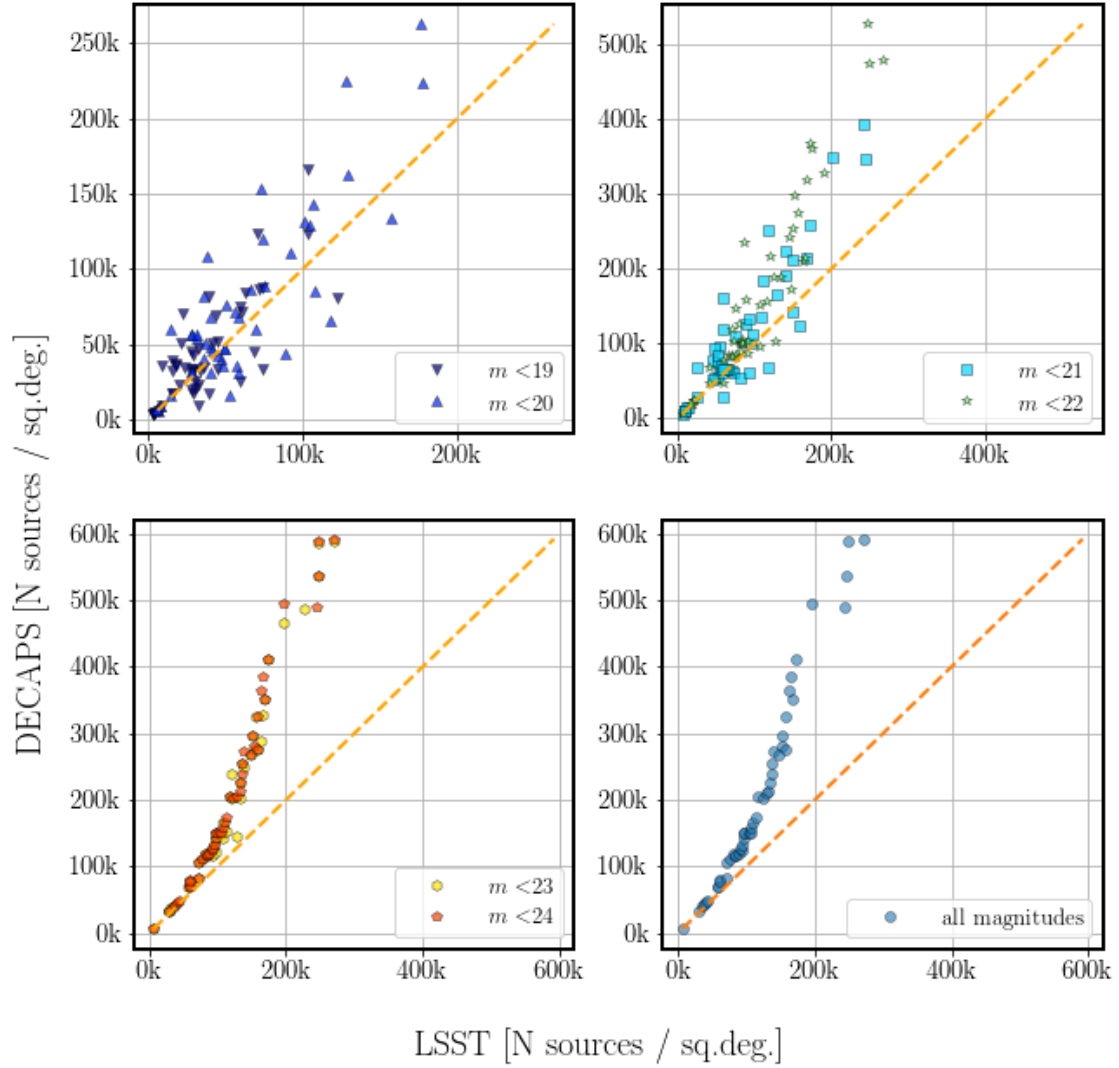
FIGURE 8: A plot of source count comparing LSST to DECAPS source catalogs of the same fields (visits) - each point per panel corresponds to a different visit. Clockwise from the upper-left panel we add progressively fainter sources, plotting the cumulative count up to a given magnitude, N(mag<cutoff).

5.1 Completeness

For any image analysis pipeline the ability to successfully detect and deblend sources would decrease as a function of increasing stellar crowdedness.

We compare LSST and DECAPS pipelines by cross-matching the source catalogs. For each DECAPS source we look for an LSST counterpart, and binning DECAPS sources along magnitudes we ask what is the completeness of LSST detections to DECAPS - what percentage of DECAPS sources has an LSST match within 0.5 ″(Fig. 9, top panel). We repeat this exercise the other way: looking for a DECAPS counterpart for each LSST source (Fig. 9, second panel). As expected, completeness decreases as a function of magnitude and increasing stellar crowdedness. We further characterize completeness by $\langle C_{18-20}\rangle$ - the mean completeness between 18-20 mag , and m_{50} - the magnitude at which completeness falls to a 50% level (see Fig. 10 - both exhibit a slight trend with stellar crowdedness. Given that the DECAPS pipeline detections are considered the gold standard, we also show that there is a very high degree of repeatability (>95%) for source detection between two epochs (Fig.11).

We illustrate on a CCD level relatively bright (18<m<20), high S/N DECAPS sources, that do not have an LSST match. In most cases we found that these sources have S/N<5 in the LSST catalog, which led to their exclusion from the analysis (see Fig. 7).

5.2 Photometry

We compare the photometric accuracy between LSST and DECAPS, and photometric repeatability within each pipeline.

Cross-matching LSST and DECAPS source catalogs, we find that the median offset is stable as a function of magnitude in range 16-20 mag, on the level < 0.1 mag (top panel of Fig. 13). The spread of magnitude difference increases as a function of magnitude (Fig. 12, and middle panel of Fig. 13), < 0.05 mag at 20 mag.

We also test the photometric repeatability (LSST-LSST, Fig. 14 or DECAPS-DECAPS, Fig. 15) cross-matching source catalogs for visits at exactly the same location, with matching exposure time and filter, representing different epochs.
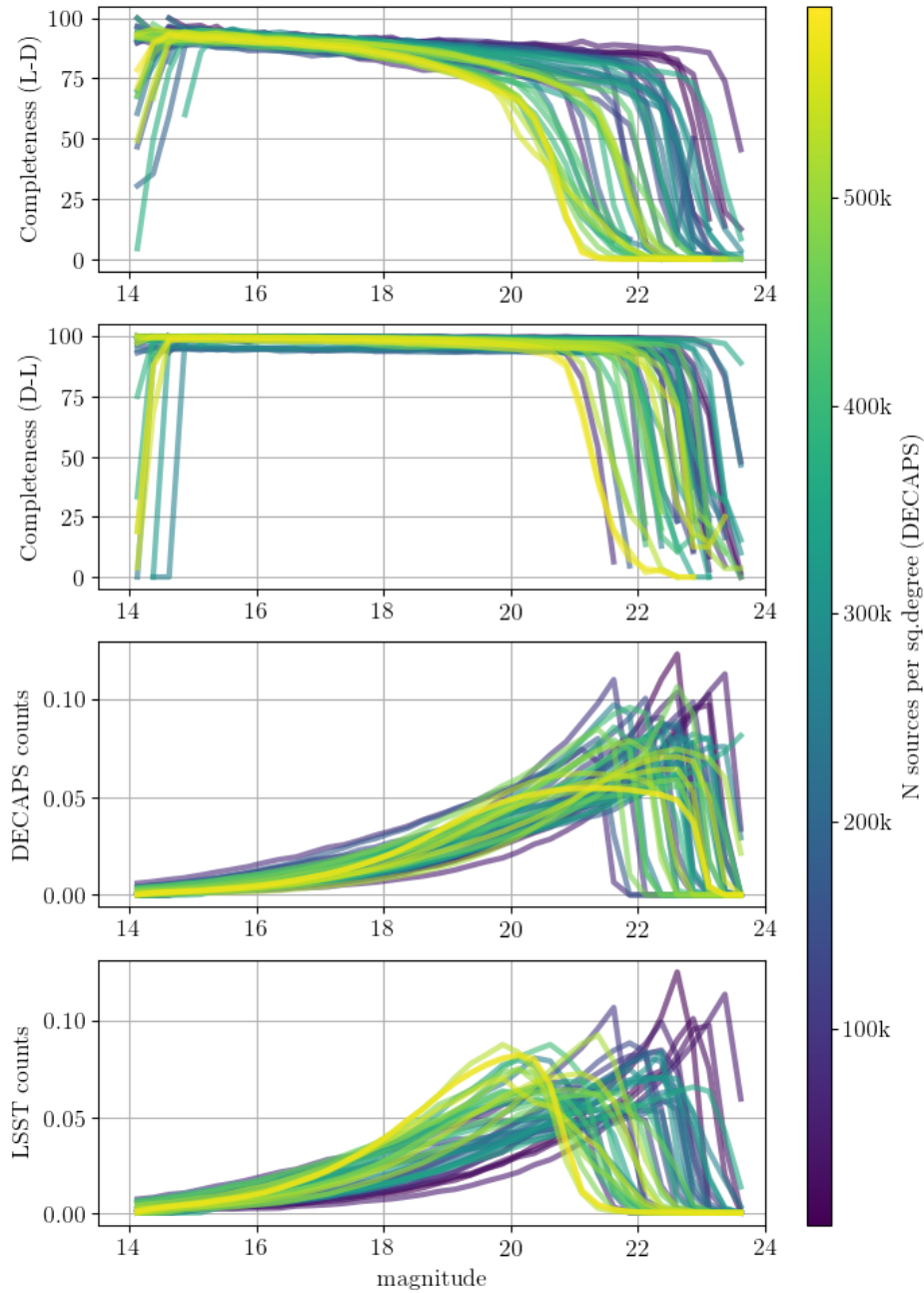
FIGURE 9: Top two panels show source-to-source completeness. The first panel is a measure of how complete is LSST catalog to DECAPS catalog (L-D), i.e. the fraction of DECAPS sources per magnitude bin that have an LSST match. The second panel shows an equivalent plot for the completeness of DECAPS to LSST (D-L), plotting the fraction of LSST sources that have a DECAPS match. The bottom two panels show the normalized source counts in the input catalogs. The LSST-DECAPS completeness falls off quicker than DECAPS-LSST, since DECAPS catalog contains more sources at fainter magnitudes (see Fig. 8). Different colors correspond to different level of stellar crowdedness, expressed in terms of the number of sources per square degree in DECAPS clean catalogs.
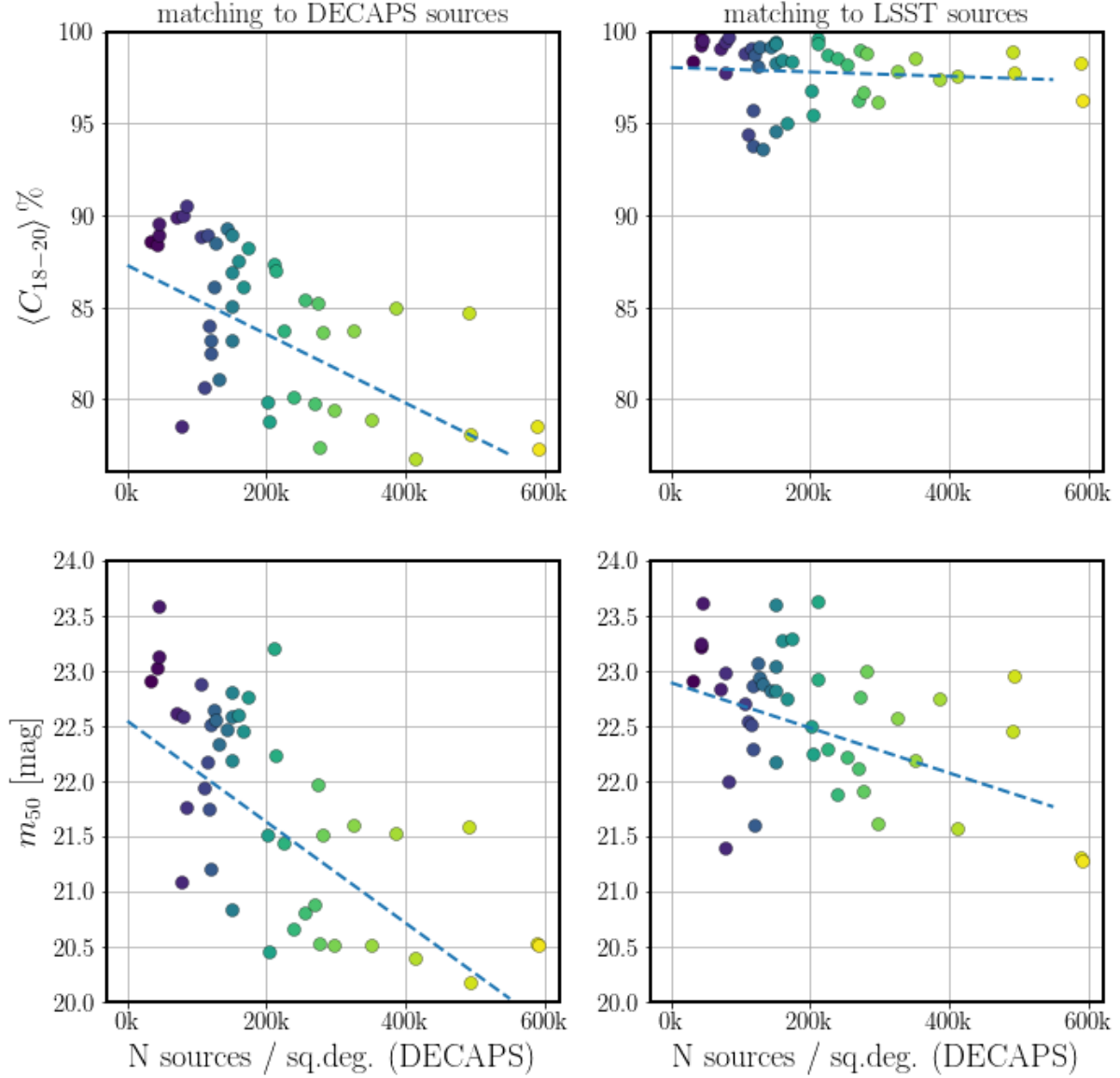
FIGURE 10: Magnitude at which completeness falls to 50% (top two panels), and the mean completeness between 18 and 20 magnitudes (bottom two panels). The panels on the left hand side correspond to the uppermost panel in Fig. 9, while the right hand side panels correspond to the second panel in Fig. 9. The color of all points corresponds to the stellar density. In each panel we overplot the linear best-fit to indicate the expected overall trend of decreasing $\langle C_{18-20} \rangle$ and m_{50} with source density.
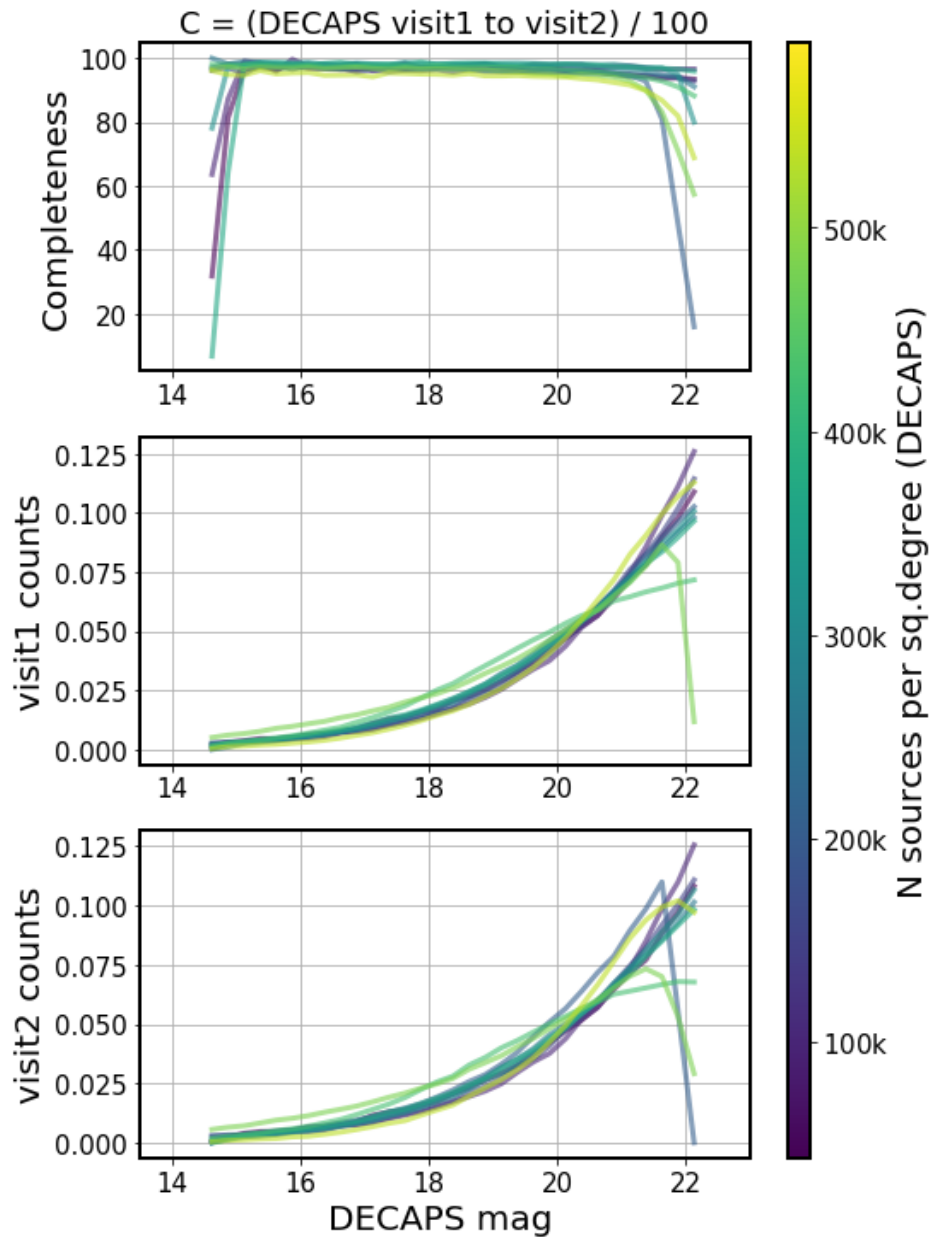
FIGURE 11: The same quantities as on Fig. 9, but corresponding to two different visits at the same location, testing the repeatability of DECAPS detections. The two visits (visit1, visit2) were chosen in the same filter and at the same location, and as in tests for completeness, we match source-by-source and consider the number of sources per magnitude bin in visit1 that do have a matching source in visit2.
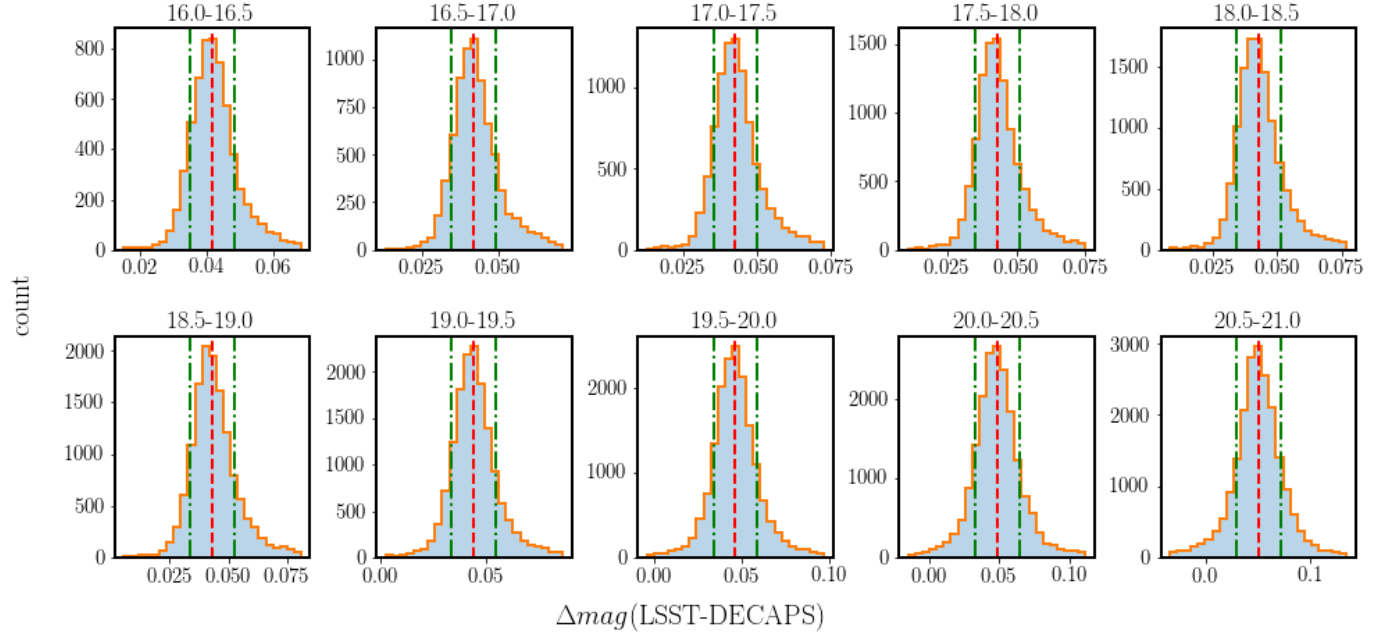
FIGURE 12: Cross-section of a difference in magnitudes between DECAPS and LSST for a visit 611970. Each panel contains the histogram of Δmag per DECAPS magnitude bin. The vertical red line corresponds to the median value of Δmag in that bin, and each histogram is limited between $\pm 4\,\sigma_G$. The vertical dot-dashed green lines mark the median $\pm \sigma_G$.

On Fig. 16 and 17 we compare the spread of photometric scatter between the two pipelines and the empirical measurement of noise from repeatability for a pair of visits at the same location.

The median error reported by either pipeline for either epoch is a measure of Poisson noise - the expected uncertainty in a repeated measurement. If e_{1L} and e_{2L} are LSST-reported error measurements for a given source for the two epochs, the quadrature-mean is

$$e_{12} = \sqrt{e_{1L}^2 + e_{2L}^2}/\sqrt{2} \tag{1}$$

The scatter between the two pipelines calculated either for epoch1 $\sigma_G(D1, L1)$, or epoch2 $\sigma_G(D2, L2)$. We find the quadrature-mean:

$$\sigma_G(DL) = \sqrt{\sigma_{D1,L1}^2 + \sigma_{D2,L2}^2}/\sqrt{2} \tag{2}$$

17

The scatter between the two epochs within the same pipeline: $\sigma_G(D1, D2)$, or $\sigma_G(L1, L2)$, consists of noise σ_E and the systematic offset σ_S :

$$\sigma_{LL}^2 = \sigma_S^2 + \sigma_E^2 \tag{3}$$

Thus we calculate the systematic offset for LSST as:

$$\sigma_S = \sqrt{\sigma_{LL}^2 - \sigma_E^2} \tag{4}$$

6 Astrometry

Astrometry pertains to the measurement of the position of sources in the absolute World Coordinate System (WCS). Accurate and precise astrometry enables catalog cross-matching, and over long-term - measurement of proper motion of stellar sources.

We consider two properties of successful astrometry. First, the internal consistency, measuring the repeatability of astrometric measurement epoch to epoch. For both LSST and DE-CAPS, we find the spread of differences in measured position among cross-matched sources : $\sigma_G(\Delta\alpha)$, $\sigma_G(\Delta\delta)$. Ideally, the median difference should be centered on 0, with the smallest possible spread, corresponding to astrometric precision.

Second - accuracy, and any biases between the LSST-DECAPS pipelines.

To test the repeatability we use pairs of observations at the same location, as in Sec. 5.2. Fig. 18 shows an example of the LSST-LSST comparison, with Fig. 19 showing the magnitude dependence. Fig. 20 depicts the offset in RA, DEC, for DECAPS-DECAPS comparison.

To test possible offset between LSST and DECAPS astrometric solutions, on Fig. 22 we find the offset in measured RA, DEC for sources cross-matched in catalogs from the two pipelines.
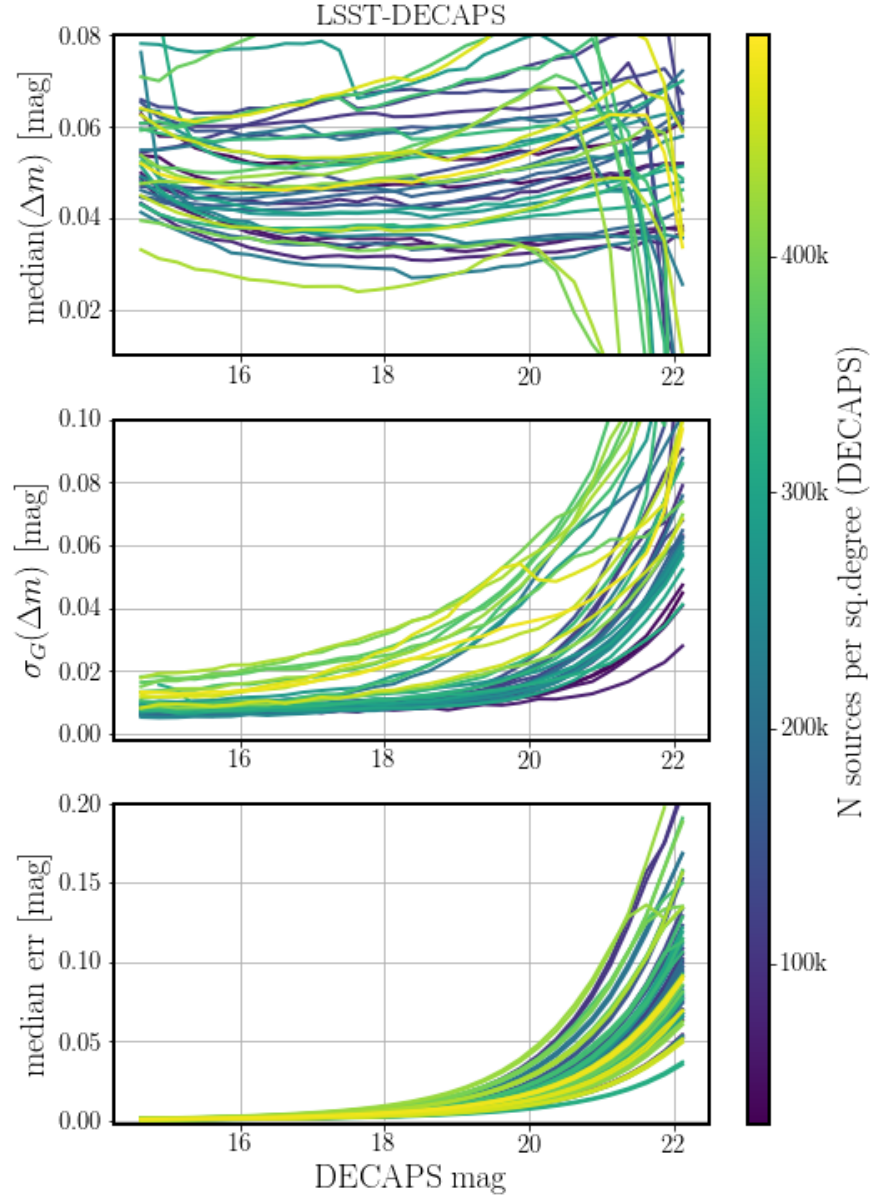
FIGURE 13: The measurement of photometric offset between DECAPS and LSST pipelines. For each visit we cross-matched source catalogs corresponding to LSST and DECAPS processing; Δm is the difference in magnitude reported between DECAPS and LSST for the same source. For each visit we bin sources according to their DECAPS magnitude. On three panels we plot the binned statistics : median(Δm), $\sigma_G(\Delta m)$, and median photometric uncertainty.
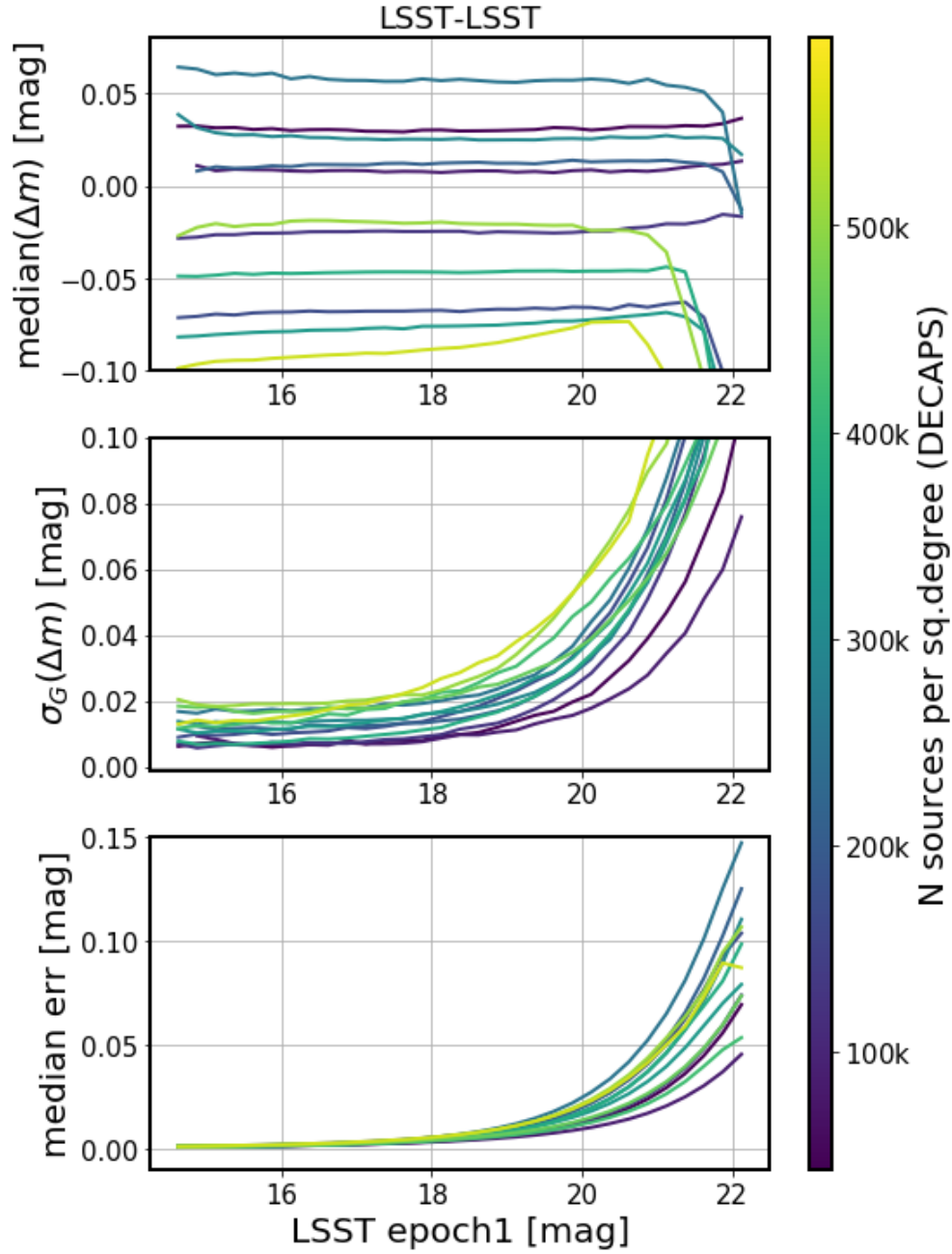
FIGURE 14: The repeatability test of the LSST pipeline. We cross-match the source catalogs for each visit. These two brightness measurements for the same source are akin to a two-epoch light curve. Since inherently variable sources constitute a small fraction of all stellar objects, and the majority of stars are not variable, the difference in the measured magnitudes would correspond to the empirical measure of noise. All sources cross-matched within 0.5″ are binned according to their brightness. On the panels we plot, from top to bottom: median photometric offset, the robust interquartile-based measure of standard deviation σ_G, and the median reported measurement uncertainty.
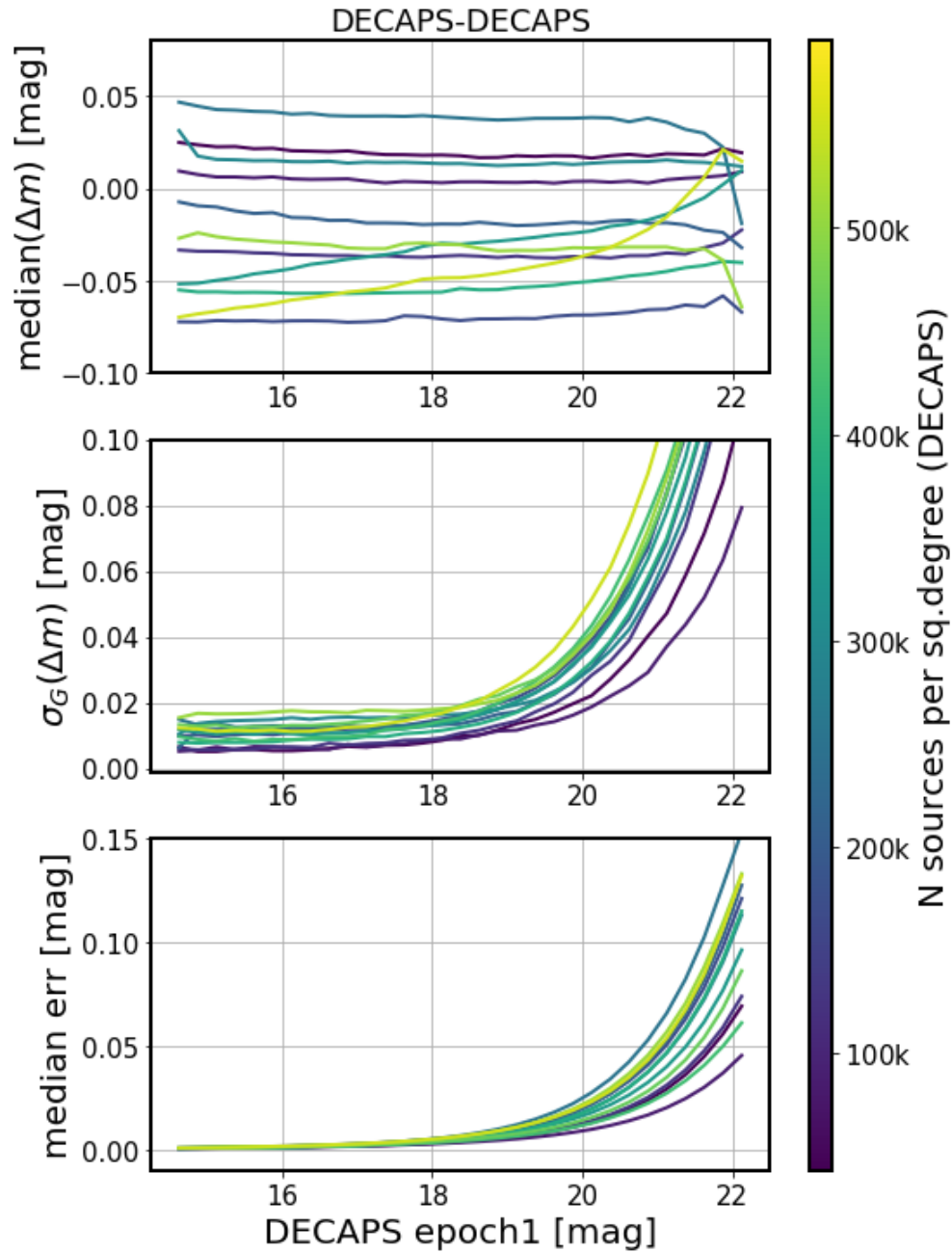
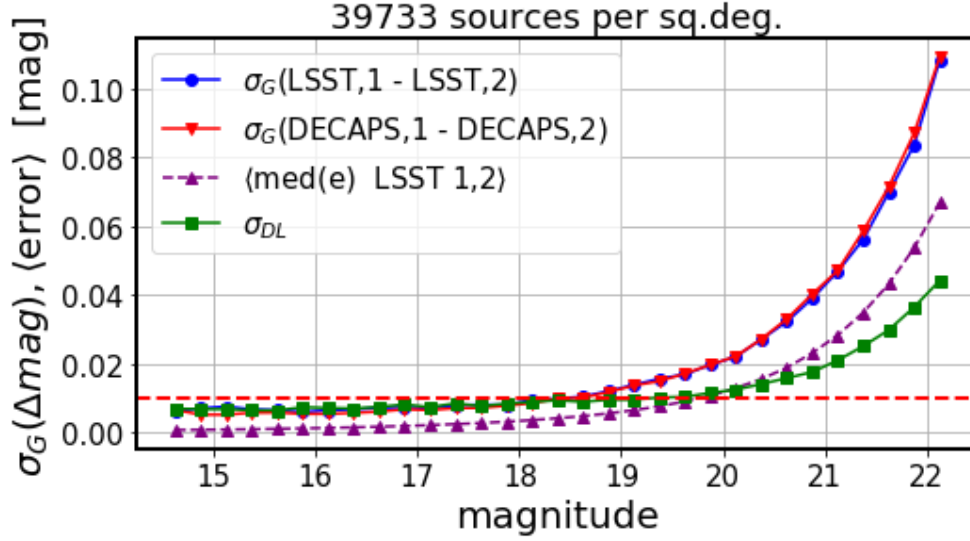FIGURE 15: The repeatability test of the DECAPS pipeline, as Fig. 14.

FIGURE 16: Analysis of the photometric spread with two visits in a low density region: 525846 (epoch1) and 530012 (epoch2). The solid blue and red lines represent the spread in photometry within each pipeline ($\sigma_G(L1, L2)$, $\sigma_G(D1, D2)$). The purple dashed line in the middle traces the average reported error between the two epochs, e_{12} (Eq. 1), which is a measure of the Poisson noise. Finally, the bottom solid green line with square markers is the spread in photometry between the two pipelines, $\sigma_G(DL)$ (Eq. 2). The difference between the purple dashed and red/blue lines is a measure of systematic noise (see Eq. 4, and Fig. 17).
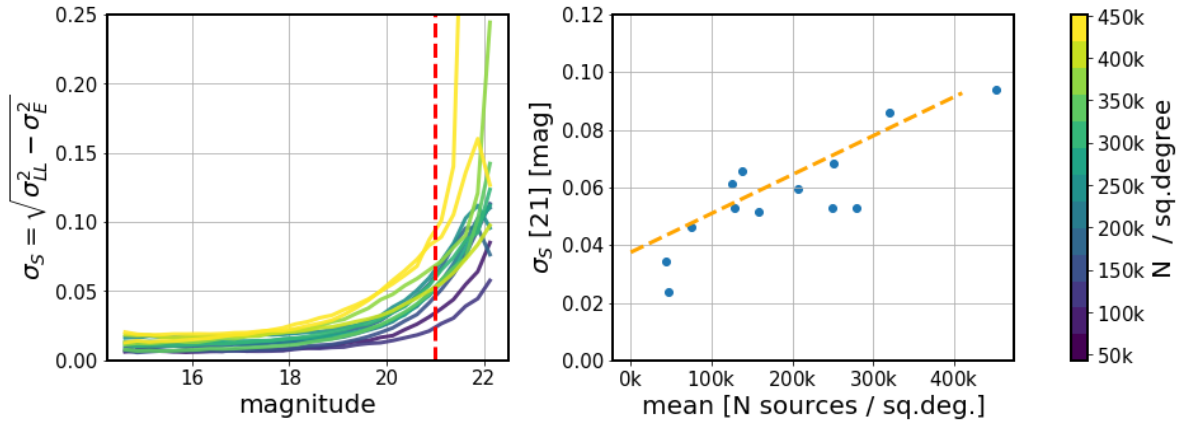

FIGURE 17: The left panel shows the measure of systematic offset between mean photometric error, and the photometric repeatability for the LSST pipeline as a function of magnitude (Fig. 16). The vertical line marks the level of 21 mag, at which we measure σ_S : $\sigma_S[21]$. The right panel shows $\sigma_S[21]$ as a function of DECAPS stellar density.
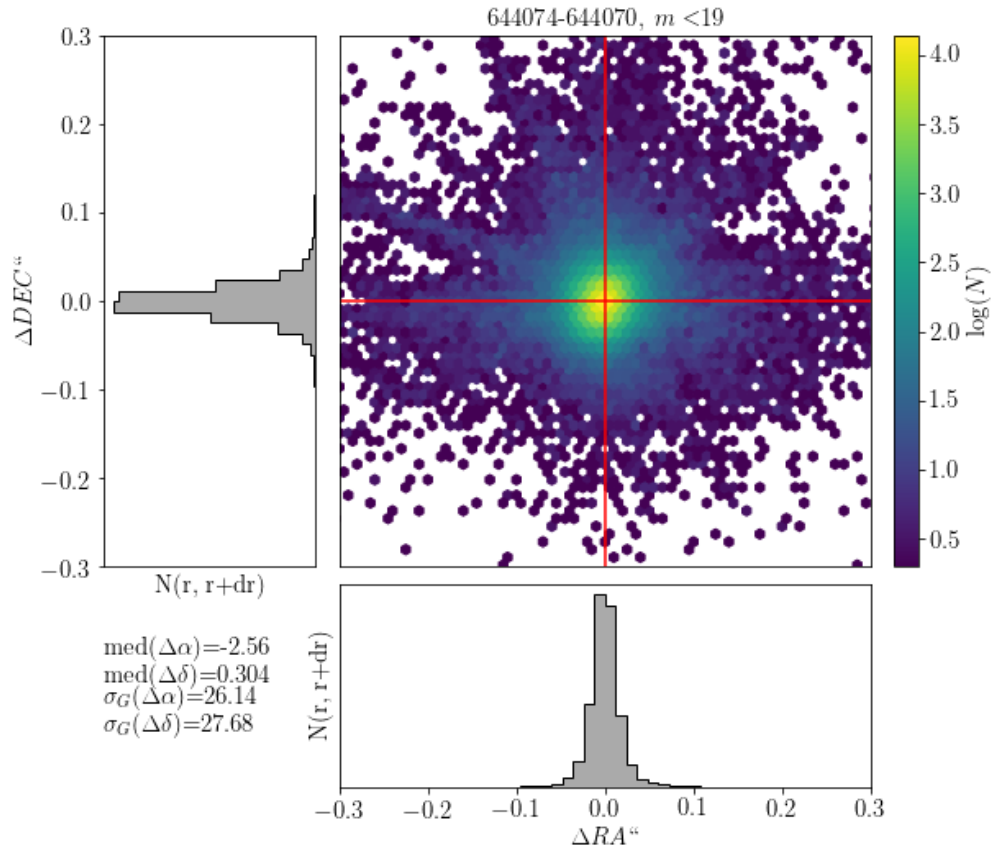
FIGURE 18: The difference of LSST processing for RA,DEC for visits 644074,644070 : a top 1% region according to Galfast, with DECAPS measured 419 000 sources per sq.deg. We select sources brighter than 19 magnitude. For all other pairs the offsets are also centered on zero with similar spread (Fig. **??**)
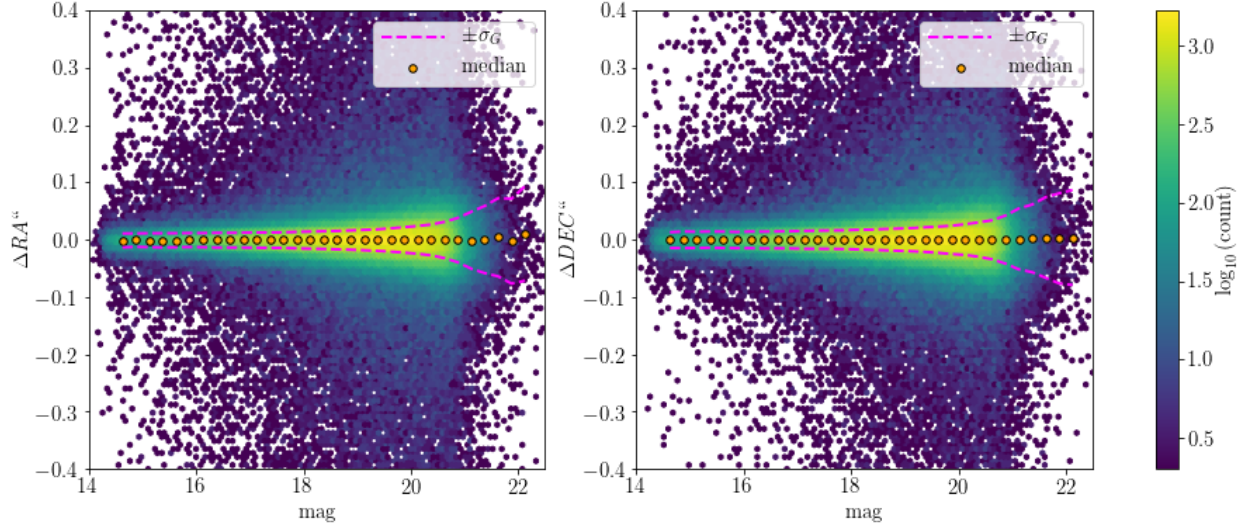
FIGURE 19: The difference in RA,DEC for the same visits as on Fig. 18, shown as a function of magnitude.

7 Conclusions

We find that the LSST image processing pipelines perform well compared to DECAPS pipelines that were specifically designed for crowded field photometry. The mean 18-20 mag completeness of LSST to DECAPS detections even at 5% density level, that approximately traces the contours of the Galactic Confusion Zone, is 85%.

Future work:

- using the simulated sky images with StarFast image simulator[14] where the true source count and position are known, rather than measured

- considering the width of the stellar locus (w-color) on the g-r s r-i diagram (Fig.2 in [?])

References

[1] Bosch, J., et al. 2017, ArXiv e-prints 1705.06766

---
[14]https://dmtn-012.lsst.io

FIGURE 20: The difference in RA,DEC for the same visits as in Fig. 18, but comparing DE-CAPS single-epoch catalogs. The spread of $\Delta\alpha$, $\Delta\delta$ is wider than for equivalent visit pairs processed by the LSST Science Pipelines - see Table **??**

FIGURE 21: Summary of LSST and DECAPS repeatability of astrometry, as in Tables **??** and **??**.
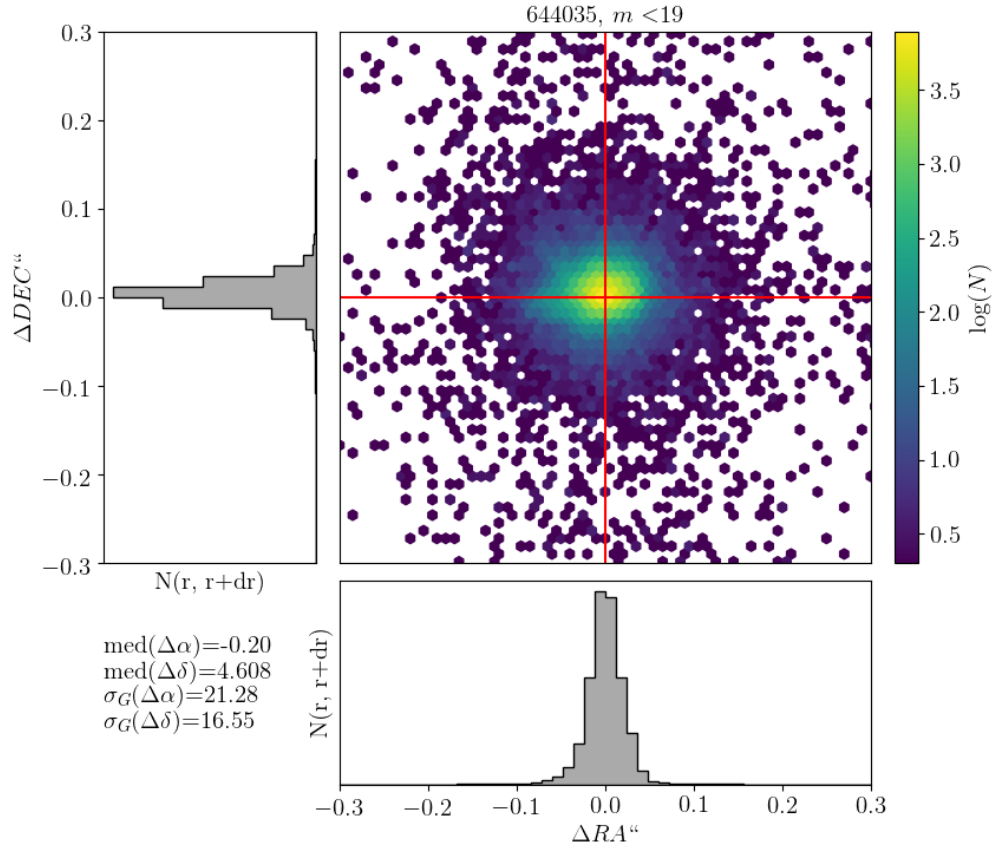
FIGURE 22: The LSST-DECAPS astrometric offset for visit 644035, with 200 000 sources per sq.deg. measured by DECAPS, in a Galfast 10% density region. In DECAPS pipeline the astrometry was tied to 2MASS-GAIA or GAIA depending on the visit number (see Fig.12 in [10]). LSST pipeline on the other hand used solely GAIA for astrometric calibration. For this visit the offset is due to precision, rather than different astrometric standards, since both DECAPS and LSST used GAIA data for astrometric calibration.

[2] Górski, K. M., Hivon, E., Banday, A. J., Wandelt, B. D., Hansen, F. K., Reinecke, M., & Bartel-mann, M. 2005, ApJ, 622, 759

[3] Hogg, D. W. 2001, The Astronomical Journal, 121, 1207

[4] Lupton, R. 2005, in prep.

[5] Lupton, R., Gunn, J. E., Ivezić, Z., Knapp, G. R., & Kent, S. 2001, in Astronomical Society of the Pacific Conference Series, Vol. 238, Astronomical Data Analysis Software and Systems X, ed. F. R. Harnden, Jr., F. A. Primini, & H. E. Payne, 269

[6] Lupton, R. H., Ivezić, Z., & Gunn, J. 2005, in prep.

[7] Lupton, R. H., Ivezić, Z., Gunn, J. E., Knapp, G., Strauss, M. A., & Yasuda, N. 2002, in SPIE Proceedings, Vol. 4836, Survey and Other Telescope Technologies and Discoveries, ed. J. A. Tyson & S. Wolff, 350

[8] Narayan, G., et al. 2018, ArXiv e-prints

[9] Olsen, K. A. G., Blum, R. D., & Rigaut, F. 2003, AJ, 126, 452

[10] Schlafly, E. F., et al. 2017, ArXiv e-prints 1710.01309

[11] Shaw, R. A. 2015, NOAO Data Handbook

[12] Stetson, P. B. 1987, PASP, 99, 191